

## Article

# Study on Temperature Characteristics of Lubrication Film of Valve Plate Pair in Axial Piston Pumps

Zhiqiang Zhang <sup>1,2,\*</sup>, Shaojie Ma <sup>1</sup>, Pingzhu Lv <sup>1</sup>, Qun Chao <sup>3</sup>, Lin Li <sup>1,2</sup>  and Zhiqi Liu <sup>1,2</sup>

<sup>1</sup> School of Mechanical Engineering, Taiyuan University of Science and Technology, Taiyuan 030024, China; s202112110435@stu.tyust.edu.cn (S.M.); s202112210530@stu.tyust.edu.cn (P.L.); lilin1991@tyust.edu.cn (L.L.); liuzhiqi@tyust.edu.cn (Z.L.)

<sup>2</sup> Shanxi Key Laboratory of Metallic Materials Forming Theory and Technology, Taiyuan University of Science and Technology, Taiyuan 030024, China

<sup>3</sup> State Key Laboratory of Mechanical System and Vibration, Shanghai Jiao Tong University, Shanghai 200240, China; chaoqun@sjtu.edu.cn

\* Correspondence: zhiqiangzhang1@tyust.edu.cn

**Abstract:** The film temperature distribution of the valve plate pair in axial piston pumps affects its lubrication, leakage, and friction. In order to investigate the film temperature distribution of the valve plate pair in axial piston pumps, a test platform was constructed including three displacement sensors for the oil film thickness and eleven thermocouples for the film temperature distribution of the valve plate pair. An accurate film shape model of the valve plate pair was built according to the three-point film thickness test data. Based on the film shape model, the film temperature model of the valve plate pair was developed considering the viscous oil temperature characteristics, the energy loss caused by leakage and viscous friction in the film, and the heat conduction among the oil, cylinder block, and valve plate. The influence of different swash plate tilt angles and operating pressures on the valve plate film temperature was studied. The test results indicate that the film temperature of the valve plate pair increases as the working pressure and swash plate tilt angle increase. The theoretical and experimental absolute errors of the film temperature in the circumferential range  $[-60^\circ, 60^\circ]$  of the valve plate high-pressure side are less than  $3.5^\circ\text{C}$ . As the swash plate tilt angle varies from  $12^\circ$  to  $16^\circ$  and working pressure from 3 MPa to 7 MPa, the minimum film thickness position and the maximum temperature point move accordingly in the circumferential range  $[-15^\circ, 5^\circ]$  of the valve plate pair.

**Keywords:** axial piston pump; valve plate; wedge angle; azimuth angle; temperature characteristics



**Citation:** Zhang, Z.; Ma, S.; Lv, P.; Chao, Q.; Li, L.; Liu, Z. Study on Temperature Characteristics of Lubrication Film of Valve Plate Pair in Axial Piston Pumps. *Appl. Sci.* **2024**, *14*, 3359. <https://doi.org/10.3390/app14083359>

Academic Editor: Nikolaos Koukouzas

Received: 25 March 2024

Revised: 13 April 2024

Accepted: 14 April 2024

Published: 16 April 2024



**Copyright:** © 2024 by the authors. Licensee MDPI, Basel, Switzerland. This article is an open access article distributed under the terms and conditions of the Creative Commons Attribution (CC BY) license (<https://creativecommons.org/licenses/by/4.0/>).

## 1. Introduction

An axial piston pump provides the benefits of high working pressure and a significant power-to-weight ratio [1]. It is commonly utilized in the military sector, ships, aviation, and construction machinery. Moreover, it can function effectively in high-pressure situations and at varying speeds [2–6]. The friction pair consisting of the piston cylinder and the valve plate in the axial piston pump is referred to as the valve plate pair. The oil film in the valve plate pair functions to seal and support the load, but it also causes energy loss, affecting the operational efficiency of the piston pump. The factors that affect the lubrication effect of the valve plate pair will result in the efficiency and sustainability of the valve plate pair. In the process of axial piston pump operation, the valve plate pair has high friction due to the influence of uneven forces and off-load moments. At the same time, in the process of work, the pollution of oil [7–9] and the selection of inappropriate oil will aggravate the friction of the valve plate pair. Aggravating the friction of the valve plate pair affects the efficiency improvement and sustainable work of the valve plate pair while generating a lot of heat, so the film temperature of the valve plate pair will rise. So, studying the temperature characteristics of the valve plate pair is quite important.

Many scholars have studied the valve plate pair. Wang et al. [10–12] studied the lubrication characteristics of the valve plate pair in an axial piston pump, obtained the oil film thickness, pressure, and temperature distribution in the valve plate pair, and analyzed the influence of wedge angle, working pressure, hydraulic oil viscosity, film thickness, and other factors on the film temperature of the valve plate pair. Tang et al. [13] established a thermal elastohydrodynamic lubrication model for slipper pairs, obtained the oil film thickness and pressure distribution of slipper pairs, and studied the influence of different working conditions and structural parameters of slipper pairs on the thermal elastohydrodynamic lubrication performance. Further work studied the power loss characteristics of the slipper pair of an axial piston pump considering thermoelastichydrodynamic deformation and optimized the structural parameters of the slipper pair [14]. J. M. Bergada et al. [15] established a set of new equations for the pressure distribution, leakage, force, and torque of the seal clearance of the discharge waist groove of the valve plate pair of an axial piston pump, in which the influences of important parameters such as wedge angle, speed, oil film thickness, and silence groove were also considered. In their further study [16], the dynamics of the cylinder block were analyzed, and the relationships between the gap film thickness of the valve plate and the oil pressure and temperature were pointed out. It showed that mixed friction between the cylinder block and valve plate occurred under certain conditions. Xu et al. [17] used a noncontact test scheme to measure the multi-freedom displacement of the cylinder block, indicating that the cylinder block real-timely fluctuates periodically in the multi-freedom displacement. Zhang et al. [18] experimentally measured the three-point oil film thickness of the valve plate pair of an axial piston pump, established the oil film shape formula, and inferred that the wedge angle of the valve plate pair was affected by multiple factors. Zhang et al. [19] proposed and verified the dynamic seventh-order model to predict the oil film thickness of the valve plate pair in an axial piston pump.

Tang et al. [20] studied the aviation axial piston pump and established the thermodynamic model of the slipper pair. The experimental and theoretical results showed that the extrusion pressure and hot wedge support force were the main factors affecting the oil film thickness and bearing capacity, and the ideal slipper radius ratio and hole length–diameter ratio were obtained by optimizing the structural parameters of the slipper and oil composition. Kazama et al. [21] took hydraulic oils with different viscosities and water–glycol hydraulic oil as test fluids and measured the temperatures of the swash plate, valve plate, and cylinder block by a thermocouple under different inlet oil temperatures and viscosities. The test results show that the temperature of the valve plate proportionately increases as the load pressure increases. Zecchi et al. [22] established a model for predicting the casing and outlet oil temperatures of an axial piston pump working stably, and the predicted value agreed with the measured results. Then, 22 thermocouples were installed on the valve plate, and the oil film temperature of the valve plate pair was measured under different working conditions [23]. L. Shang et al. [24] also proposed a temperature prediction model considering hydraulic oil compression and expansion, the heat transfer caused by energy loss and power loss, and the temperature change of the pump outlet and shell was well predicted. Chacon et al. [25] proposed a thermoelastohydrodynamic model to solve the pressure and temperature distribution in a fluid film, the temperature distribution in a solid, and its elastic deformation under the influence of pressure and heat. Petrovic et al. [26] studied the working performance, efficiency, and reliability of CPAP and analyzed the effect of temperature on the pump efficiency by taking into account the viscosity of hydraulic oil.

To improve film temperature model accuracy, a shape model of the oil film of a valve plate pair is developed according to the test data of the three-point oil film thickness of the valve plate pair. On this basis, an oil film temperature distribution model is established, considering the viscous oil temperature characteristics, the energy loss caused by leakage and viscous friction in the film, and the heat conduction among the oil, cylinder block, and valve plate. A test platform is built, in which three displacement sensors for film thickness are installed in the low-pressure side of the valve plate and eleven thermocouples for film

temperature are laid in the high-pressure side of the back of the valve plate. According to the theoretical and test data, the film temperature distribution of the valve plate pair in an axial piston pump is studied. Assume that the speed of the axial piston pump is always 1000 rpm.

## 2. Modeling

### 2.1. Modeling of Lubricating Film Shape

Figure 1 shows the general configuration of a CY swash plate-type axial piston pump, comprising a main shaft, swash plate, cylinder block, pistons, and valve plate, among other components. In the pump, the cylinder block rotates relative to the valve plate fixed on the front housing. The Cartesian coordinate system is established in Figure 2. The origin  $O_c$  of the coordinate system is located at the intersection point of the spindle axis and the top surface of the valve plate. The  $Y_c$ -axis points towards the outlet port, and the  $Z_c$ -axis coincides with the center line of the spindle and points towards the right side of the spindle in Figure 1. The wedge angle  $\alpha$  is the angle between the valve plate and the cylinder block, while the azimuth angle  $\gamma$  is the angle between the  $Y_c$ -axis and the line between the minimum-film-thickness point and the origin  $O_c$ . The positive direction is specified as clockwise in Figure 2.

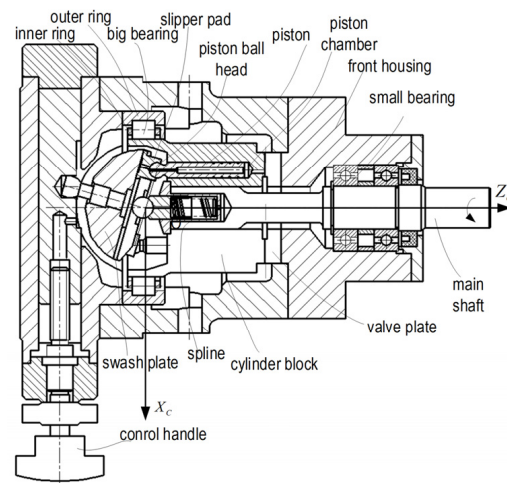


**Figure 1.** Structure of the axial piston pump.

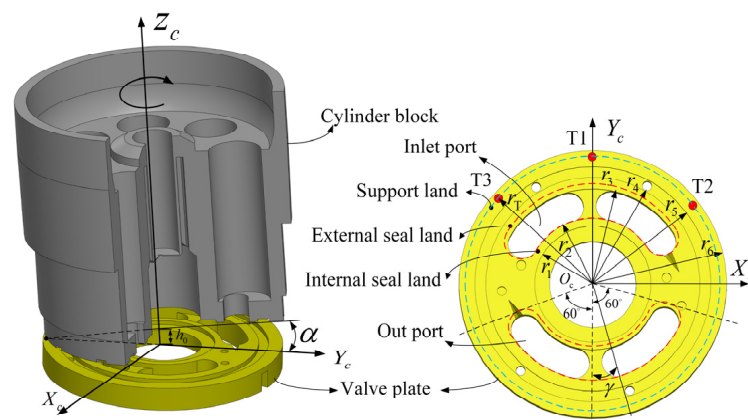


**Figure 2.** The wedge lubrication film between the cylinder block and valve plate.

The cylinder block tilts relative to the valve plate under the influences of several factors, mainly including the forces acting on the cylinder block and torques due to the forces, eccentric wear of the valve plate, and the coaxiality error between the main shaft and the cylinder block [27].

### (1) Modeling of the force balance of the cylinder block

The cylinder block mainly endures three kinds of forces in the  $Z_C$  coordinate direction, which are the force  $F_{pis}$  in the negative direction due to the static pressure in piston chambers, the force  $F_{fm}$  in the positive direction caused by the static pressure in the lubrication film between the cylinder block and valve plate, and the supporting force  $F_{mix}$  in the positive direction generated by the mixed-friction contact between the cylinder block and valve plate. The cylinder block is in a force balance along the  $Z_C$ -axis direction.

The force  $F_{pis}$  is

$$F_{pis} = \frac{Z}{2} A_{pis} P_p \quad (1)$$

where  $Z$  is the number of pistons,  $A_{pis}$  is the bottom area of the piston, and  $P_p$  is the working pressure.

The force  $F_{fm}$  is

$$F_{fm} = \frac{1}{4} \left[ \frac{r_4^2 - r_3^2}{\ln(r_4/r_3)} - \frac{r_2^2 - r_1^2}{\ln(r_2/r_1)} \right] \left( \pi - \frac{2\pi}{Z} + \eta_0 \right) P_p \quad (2)$$

where  $r_1$  is the inner diameter of the inner sealing belt of the valve plate,  $r_2$  is the outer diameter of the inner sealing belt of the valve plate,  $r_3$  is the inner diameter of the outer sealing belt of the valve plate,  $r_4$  is the outer diameter of the outer sealing belt of the valve plate, and  $\eta_0$  is the central angle occupied by the discharge waist groove.

The cylinder block tilts slightly relative to the valve plate, and both of them make contact in the surrounding area of the minimum-film-thickness point. Mixed friction occurs in the area, and the micro-convex bodies in that area contact each other to generate the supporting force. The bearing capacity  $W$  and the supporting force  $F_{mix}$  in the mixed-friction area between the cylinder block and valve plate are calculated as follows:

$$\begin{cases} W = \frac{4}{3} n_f E_e R_e^{0.5} \int_h^\infty (Z_f - h)^{1.5} e^{-Z_f/\sigma_e} dz_f \\ E_e = 1 / [(1 - \gamma_1^2)/E_1 + (1 - \gamma_2^2)/E_2] \end{cases} \quad (3)$$

$$F_{mix} = \int_{\theta_i}^{\theta_j} \int_{r_5}^{r_6} W dr d\theta \quad (4)$$

where  $n_f$  is the contact number of micro-convex bodies per unit area,  $z_f$  is the maximum height of the micro-convex body,  $\sigma_e$  is the surface roughness measured by the surface profiler, and  $R_e$  is the equivalent radius of the micro-convex body at the contact interface.  $\theta_i$  and  $\theta_j$  are the angles of both ends of the mixed-friction area,  $E_1$  and  $E_2$  are the elastic modulus of the valve plate and cylinder block, respectively, and  $E_e$  is the equivalent elastic modulus.  $\gamma_1$  and  $\gamma_2$  are the Poisson ratio of the valve plate and the cylinder block, respectively, and  $h$  is the oil film thickness.

The force balance equation in the  $Z_C$ -axis direction of the cylinder block is as follows:

$$F_{pis} - F_{fm} - F_{mix} = 0 \quad (5)$$

### (2) Modeling of the film thickness between the cylinder block and valve plate

The three film thickness curves T1, T2, and T3 in Figure 3 are obtained at the three test points T1, T2, and T3 of the valve plate in Figure 2 in the experiment. The average value  $M_i$  and amplitude  $H_i$  of the three film thickness curves T1, T2, and T3, respectively, are as follows:

$$M_i = \Lambda \cdot \frac{\sum_{j=1}^n T_j}{n}, i = 1, 2, 3 \quad (6)$$

$$H_i = \Gamma \cdot \frac{T_{jmax} - T_{jmin}}{2}, i = 1, 2, 3 \quad (7)$$

where  $\Lambda$  and  $\Gamma$  are the correction coefficients,  $T_j$  is the film thickness data collected by displacement sensors at each of the three test points T1, T2, and T3,  $n$  is the number of film thickness data,  $T_{j\max}$  is the maximum value of  $T_j$ , and  $T_{j\min}$  is the minimum value of  $T_j$ .

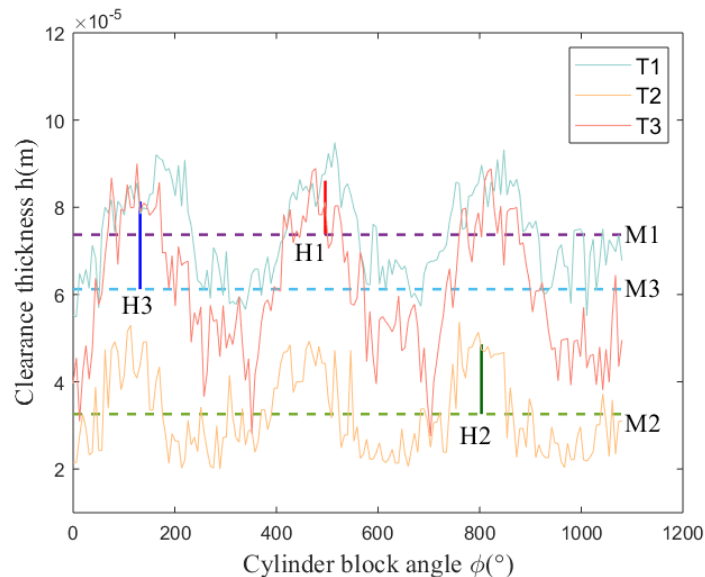


**Figure 3.** Three-point film thickness test curves.

The average value  $M_i$  of the film thickness is affected by the forces on the cylinder block, the torques on that due to the forces, and the eccentric wear of the valve plate [27], which are called the constant factors. The film thickness  $h_m$  at any point in the lubrication film by the constant factors is expressed as follows:

$$h_m = h_{0m} - \alpha_m r \cos(\theta + \gamma_m) \quad (8)$$

where  $h_{0m}$  is the central thickness of the oil film due to the constant factors,  $\alpha_m$  and  $\gamma_m$  are the wedge angle and the azimuth angle by the constant factors, respectively,  $r$  is the radius of any point in the lubrication film, and  $\theta$  is the angle between the radius line of the point and the radius line of the minimum-film-thickness point.

The film thickness curves in Figure 3 change periodically with the rotation of the cylinder block, and their amplitudes  $H_i$  ( $i = 1, 2, 3$ ) are caused by the coaxiality error between the main shaft and cylinder block [27], which is named the fluctuation factor. The red, blue and green vertical lines in the figure are the amplitudes of the three displacement curves respectively. The film thickness  $h_w$  at any point in the lubrication film by the fluctuation factor is expressed as follows:

$$h_w = h_{0w} - \alpha_w r \cos(\theta + \gamma_w) \quad (9)$$

where  $h_{0w}$  is the displacement caused by fluctuation factors,  $\alpha_w = \arctan(h_{0w}/r_6)$ ,  $\gamma_w = \varphi - \pi/2$ , and  $\varphi$  is the rotation angle of the cylinder block.

The film thickness  $h_{mw}$  at any point in the lubrication film by the constant factors and the fluctuation factor is expressed as follows:

$$h_{mw} = h_m + h_w \quad (10)$$

In Figure 4, the film thicknesses of three points  $M_1, M_2, M_3$  can determine one plane, and the average values  $M_i$  ( $i = 1, 2, 3$ ) of the film thickness at the three test points T1, T2, and T3 in Formula (9) are substituted into Formula (6) and sorted as follows:

$$\begin{cases} (M_1 - M_3) \left[ \cos\left(\frac{4\pi}{3} - \gamma_m\right) - \cos(\pi - \gamma_m) \right] - (M_1 - M_2) \\ \left[ \cos\left(\frac{2\pi}{3} - \gamma_m\right) - \cos(\pi - \gamma_m) \right] = 0 \\ (M_1 - M_3) - \alpha_m \cdot r \cdot \left[ \cos\left(\frac{2\pi}{3} - \gamma_m\right) - \cos(\pi - \gamma_m) \right] = 0 \\ M_1 - h_{0m} + \alpha_m \cdot r \cdot \cos(\pi - \alpha_m) = 0 \end{cases} \quad (11)$$

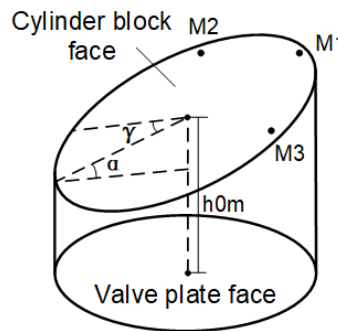


**Figure 4.** Schematic diagram of the oil film shape according to the three-point film thickness.

The values  $\alpha_m$  and  $\gamma_m$  can be obtained in Formula (11) and are substituted into the force balance Equations (1)–(5), and  $h_{0min}$  can be obtained. Then, by substituting  $h_{0min}$  into Formula (8),  $h_{mw}$  is calculated. The total film thickness  $h_{tol}$  at any point in the lubrication film is as follows:

$$h_{tol} = h_{mw} - h_{mw\_min} + h_{0min} \quad (12)$$

where  $h_{mw\_min}$  is the minimum value of  $h_{mw}$ .

Figure 5 shows the calculation process schematic diagram for the wedge angle and azimuth angle. The wedge angle and the azimuth angle at any point in the lubrication film caused by the constant factors and fluctuation factors respectively are called the total wedge angle  $\alpha_{tol}$  and the total azimuth  $\gamma_{tol}$ , respectively, which are expressed as follows:

$$\alpha_{tol} = (h_{tolmax} - h_{tolmin}) / 2r \quad (13)$$

$$\gamma_{tol} = -\pi + \frac{\pi}{180} \cdot L(h_{tolmin}) \quad (14)$$

where  $h_{tolmax}$  is the maximum value of  $h_{tol}$ ,  $h_{tolmin}$  is the minimum value of  $h_{tol}$ , and  $L(h_{tolmin})$  is the position of the minimum-film-thickness point with the valve of  $h_{tolmin}$  in the circumferential direction of the valve plate.

## 2.2. Modeling of Film Temperature

To calculate the leakage of the wedge film in Figure 6, the wedge film between the cylinder block and valve plate can be divided into the parallel part and the wedge part; therefore, the leakage of the wedge film includes the leakage  $Q_p$  of the parallel part and the leakage  $Q_w$  of the wedge part [28].

The leakage  $Q_p$  of the parallel part is

$$Q_p = \frac{\alpha_1 h_1^3 \Delta P}{12\mu C_e \ln(r_i/r_j)} \quad (15)$$

where  $\alpha_1$  is the central angle of the parallel part,  $h_1$  is the height of the parallel gap,  $\Delta P$  is the difference between the working pressure  $P_p$  and the oil pressure  $P_{out}$  in the shell,  $\mu$  is the dynamic viscosity of oil,  $C_e$  is the correction factor and the value is 2.2, and  $r_i$  and  $r_j$  are the outer and inner diameters of the calculated parallel part, respectively. For the inner sealing belt,  $r_i = r_2$  and  $r_j = r_1$ ; for the outer sealing belt,  $r_i = r_4$  and  $r_j = r_3$ ; for the auxiliary support belt,  $r_i = r_6$  and  $r_j = r_5$ .

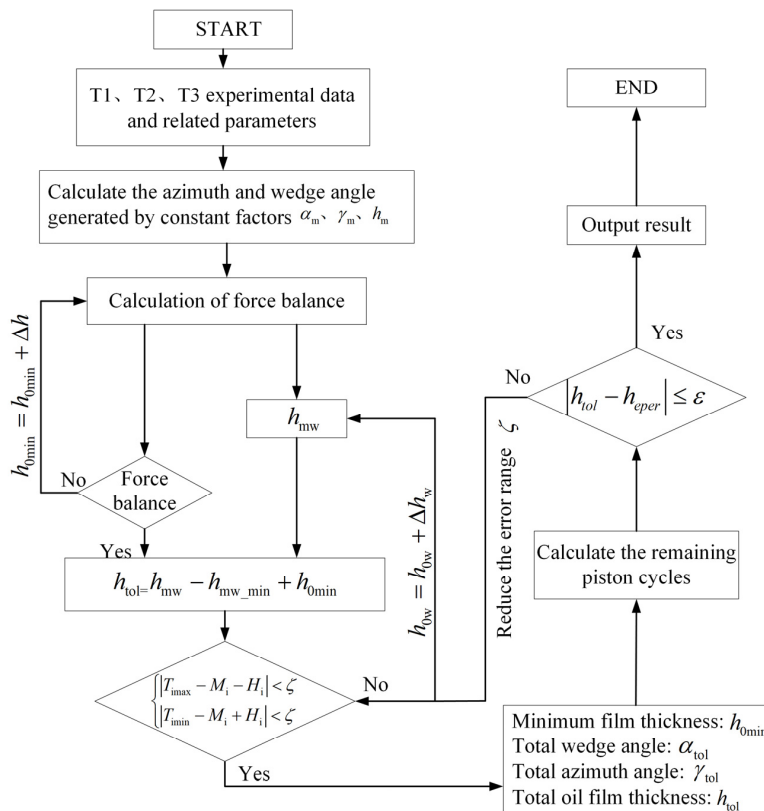


**Figure 5.** The calculation process schematic diagram for the wedge angle and azimuth angle.

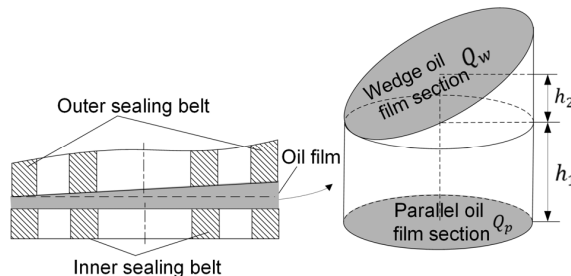


**Figure 6.** Schematic diagram of the wedge gap of the valve plate pair.

The leakage  $Q_w$  of the wedge part is as follows:

$$\left\{ \begin{array}{l} Q_w = \frac{\Delta P / 6\mu C_e}{A_1 - B_1 - C_1 - D_1} \\ A_1 = (b^2 / a^3) \ln(r_i - r_j) \\ B_1 = (b^2 / a^3) \ln[(r_i - b/a) / (r_j - b/a)] \\ C_1 = (b/a^2)(r_i^3 - r_j^3) \\ D_1 = (1/2a)(r_i^2 - r_j^2) \end{array} \right. \quad (16)$$

where  $a = 1/2[\tan^2 \alpha h_2(\alpha_1 + \sin \alpha_1)]$ ,  $b = \tan^3 \alpha \sin(\alpha_1/2)$ , and  $h_2$  is the center height of the wedge film.

The power loss  $E_L$  caused by the film leakage between the cylinder block and the valve plate is as follows:

$$E_L = (Q_P + Q_W)P_P \quad (17)$$

The tangential friction resistance results in viscous friction power loss in the lubrication film because of the high-speed rotation of the cylinder block relative to the valve plate. In

order to simplify the calculation, the oil in the valve plate film is regarded as the flow in the parallel gap, as shown in Figure 7. And the friction power loss  $E_V$  is

$$E_V = \int_{\theta_1}^{\theta_2} \int_{r_i}^{r_j} \frac{\mu \omega^2 r^3}{h} dr d\theta \quad (18)$$

where  $\omega$  is the angular velocity of the cylinder block.

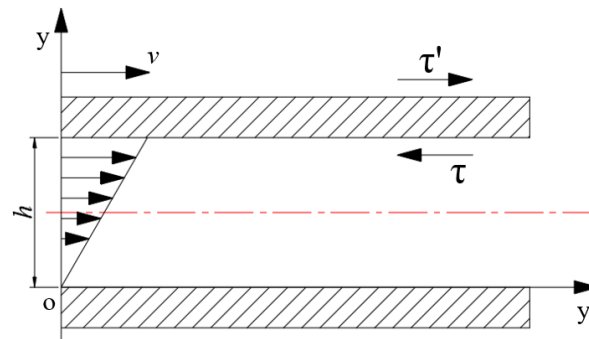


**Figure 7.** Schematic diagram of viscous friction between two parallel panels.

Thermal interaction occurs between the lubrication film and the contact parts including the valve plate, cylinder block, and the inlet oil after cooling. In Figure 8, the heat interaction occurs between the oil film and the valve plate, and its heat interaction rate  $Q_{vlp}$  is as follows:

$$Q_{vlp} = \frac{T_1 - T_0}{\frac{1}{\lambda_0 A_{vlp}} + \frac{L}{k_1 A_{vlp}} + \frac{1}{\lambda_1 A_{vlp}}} \quad (19)$$

where  $T_1$  is the oil film temperature,  $T_0$  is the starting temperature of the valve plate,  $\lambda_0$  is the heat transfer coefficient between the oil film and the valve plate,  $\lambda_1$  is the heat transfer coefficient between the oil film and the cylinder block,  $A_{vlp}$  is the heat transfer area between the valve plate and the oil film,  $k_1$  is the heat transfer coefficient of the valve plate material, and  $L$  is the thickness of the valve plate.

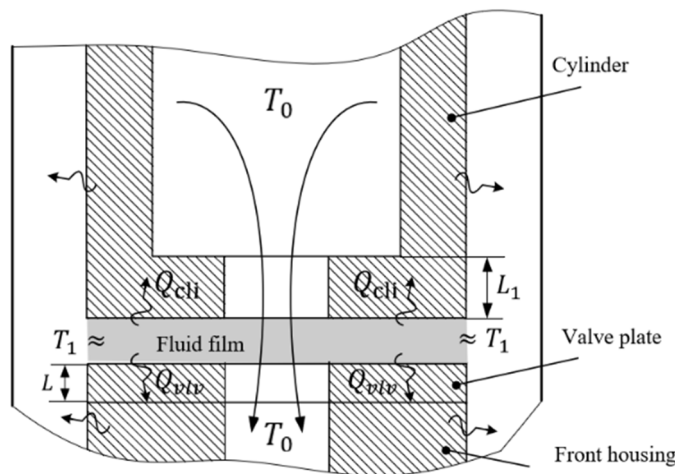


**Figure 8.** Heat transfer model in the oil film.

The heat interaction rate  $Q_{cli}$  between the oil film and the cylinder block is as follows:

$$Q_{cli} = \frac{T_1 - T_0}{\frac{1}{\lambda_0 A_{cli}} + \frac{L_1}{k_2 A_{cli}} + \frac{1}{\lambda_1 A_{cli}}} \quad (20)$$

where  $A_{\text{cli}}$  is the heat transfer area between the cylinder block and the oil film,  $k_2$  is the thermal conductivity of the cylinder block material, and  $L_1$  is the thickness of the cylinder block.

The heat interaction rate  $Q_{\text{oil}}$  between the oil film and the inlet oil after cooling is as follows:

$$Q_{\text{oil}} = k_3 2\pi r h (T_1 - T_0) \quad (21)$$

The heat flow diagram of the oil film temperature of the valve plate pair is shown in Figure 9. The oil film temperature considering the above factors can be expressed as follows:

$$T_1 = \frac{(E_L + E_V) - Q_{\text{oil}}}{\rho C_0 (Q_{\text{vlv}} + Q_{\text{cli}})} + T_0 \quad (22)$$

where  $k_3$  is the thermal conductivity of the hydraulic oil.

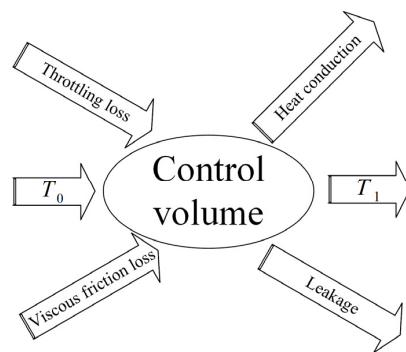


**Figure 9.** Distribution of oil film heat flow diagram.

Mobil 46# anti-wear hydraulic oil is selected as the working medium, and the relationship between viscosity and temperature is shown in Table 1.

**Table 1.** Relationship between viscosity and temperature.

Temperature (°C)	20	30	40	50	60	70	80	90	100
Viscosity (10 <sup>-2</sup> Pa·s)	11.19	6.19	3.77	2.49	1.75	1.29	1.00	0.81	0.67

Considering the influence of oil temperature on oil viscosity, the viscosity–temperature characteristic model is as follows:

$$\mu = 1560 T_{\text{vis}}^{-1.644} \quad (23)$$

where  $T_{\text{vis}}$  is the hydraulic oil temperature.

Due to a temperature shift in the circumferential direction of the valve plate, heat conduction occurs from the high-temperature area to the low-temperature area in the interior of the valve plate. The change term of the temperature inside the valve plate with time is introduced and expressed in the Cartesian coordinate system:

$$\rho_{\text{vlv}} c_p \frac{\partial T}{\partial t} = \lambda_{\text{vlv}} \left( \frac{\partial^2 T}{\partial x^2} + \frac{\partial^2 T}{\partial y^2} + \frac{\partial^2 T}{\partial z^2} \right) + q \quad (24)$$

where  $\rho_{\text{vlv}}$  is the density of the plate,  $c_p$  is the specific heat capacity,  $\lambda_{\text{vlv}}$  is the heat transfer coefficient of the plate,  $T$  is the temperature,  $q$  is the heat source term, and  $t$  is the time.

The heat conduction equation in cylindrical coordinates is as follows:

$$\rho_{\text{vlv}} c_p \frac{\partial T}{\partial t} = \lambda_{\text{vlv}} \left( \frac{\partial^2 T}{\partial r^2} + \frac{1}{r} \frac{\partial T}{\partial r} + \frac{1}{r^2} \frac{\partial^2 T}{\partial \theta^2} + \frac{\partial^2 T}{\partial z^2} \right) + q \quad (25)$$

Using the finite difference method to solve the heat conduction Equation (25), the heat conduction equation after discretization is as follows:

$$T_{i,j,k}^{p+1} = T_{i,j,k}^p - (2A_1 + B_1 + 2C_1 + 2D_1)T_{i,j,k}^p + (A_1 - B_1)T_{i+1,j,k}^p + A_1 T_{i-1,j,k}^p + C_1(T_{i,j-1,k}^p + T_{i,j+1,k}^p) + D_1(T_{i,j,k+1}^p + T_{i,j,k-1}^p) + E_1 \quad (26)$$

where  $A_1$ ,  $B_1$ ,  $C_1$  and  $D_1$  are, respectively, represented as follows:

$$A_1 = \frac{\lambda_{\text{vlv}} \Delta t}{\rho_{\text{vlv}} c_p \Delta r^2} \quad (27)$$

$$B_1 = \frac{\lambda_{\text{vlv}} \Delta t}{\rho_{\text{vlv}} c_p r \Delta r} \quad (28)$$

$$C_1 = \frac{\lambda_{\text{vlv}} \Delta t}{\rho_{\text{vlv}} c_p r^2 \Delta \theta^2} \quad (29)$$

$$D_1 = \frac{\lambda_{\text{vlv}} \Delta t}{\rho_{\text{vlv}} c_p \Delta z^2} \quad (30)$$

$$E_1 = \frac{q \Delta t}{\rho_{\text{vlv}} c_p} \quad (31)$$

### 2.3. Numerical Calculation

According to the calculation flow chart shown in Figure 10, the MATLAB (9.7.0.1190202 (R2019b)) program was used to numerically calculate the film temperature distribution of the valve plate auxiliary support belt in the axial piston pump. The relevant parameters of the axial piston pump are shown in Table 2.

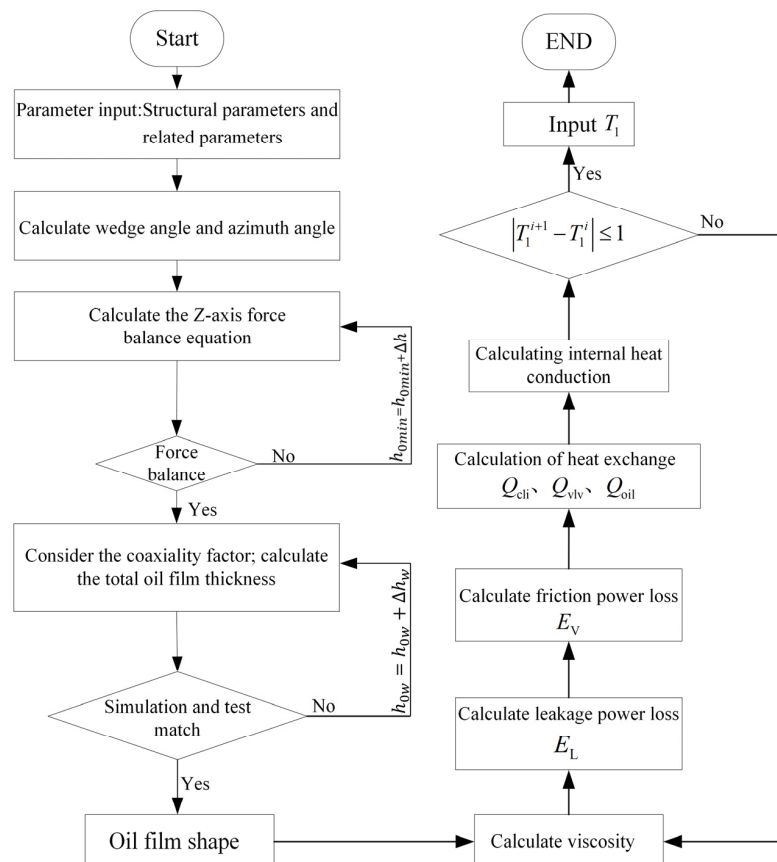


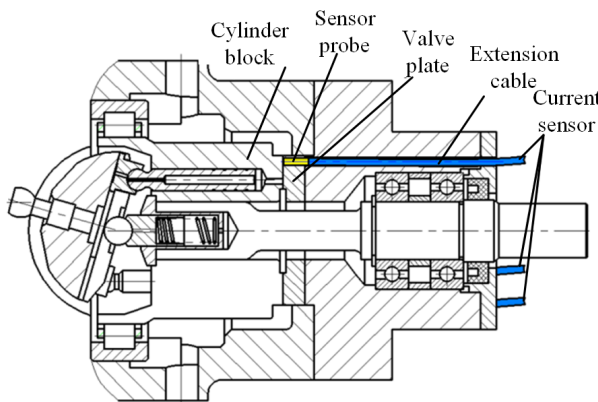
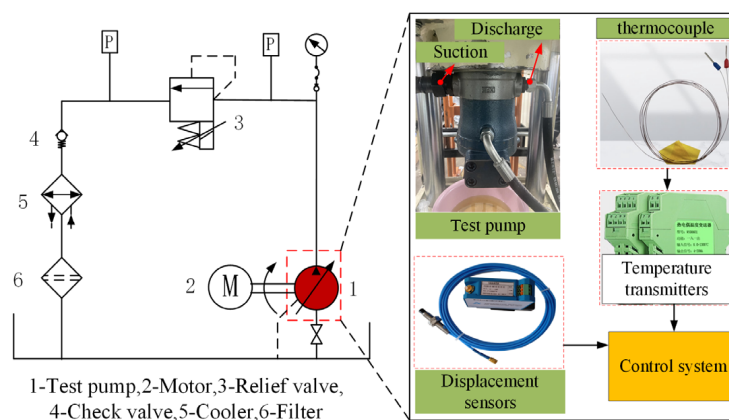
**Figure 10.** Diagram of numerical calculation program.

**Table 2.** Key parameters of axial piston pump.

Name	Parameter	Name	Parameter
$r_1$ (mm)	18.44	$h_{0w}$ ( $\mu\text{m}$ )	10
$r_2$ (mm)	21.38	Z	7
$r_3$ (mm)	30.47	$\rho$ ( $\text{Kg}/\text{m}^3$ )	870
$r_4$ (mm)	33.44	$q$ ( $\text{mL}/\text{r}$ )	40
$r_5$ (mm)	37.50	P (MPa)	31.5
$r_6$ (mm)	42.50	n (rpm)	1000
$n_f$ ( $\mu\text{m}^{-2}$ )	0.1454		

### 3. Experiment

The film temperature test scheme of the axial piston pump is shown in Figures 11 and 12. Figure 11 shows the installation diagram of three eddy current displacement sensors, which were used to measure the gap between the valve plate and cylinder block [29]. The installation position points of the three displacement sensors are T1, T2, and T3 in Figure 2, respectively. T1, T2, and T3 are located at the low-pressure side of the valve plate, and the radius of the circle  $r_T$  is 38.1 mm.

**Figure 11.** Eddy current transducer installation positions.**Figure 12.** Schematic diagram of the test.

As shown in Figure 12, the oil film thickness signals at the three measurement points T1, T2, and T3 were imported into the computer through the preamplifier and the data acquisition card. The film thickness and temperature distribution data were obtained at four working conditions. In working condition 1, the pump working pressure is 3 MPa, and the swash plate tilt angle is  $12^\circ$ . In working condition 2, the pump working pressure is 3 MPa, and the swash plate tilt angle is  $16^\circ$ . In working condition 3, the pump working

pressure is 7 MPa, and the swash plate tilt angle is  $12^\circ$ . In working condition 4, the pump working pressure is 7 MPa, and the swash plate tilt angle is  $16^\circ$ . The pump rotation speed at working conditions 1~4 is 1000 r/min.

#### 4. Results and Discussion

##### 4.1. Comparison of Theoretical Curve and Experimental Curve of Three-Point Film Thickness

The oil film thickness data at T1, T2, and T3 in Figure 2 were substituted into the wedge film shape model of the valve plate pair in Section 2.1. The theoretical film thickness curves at the three points were obtained and are shown in Figure 13.

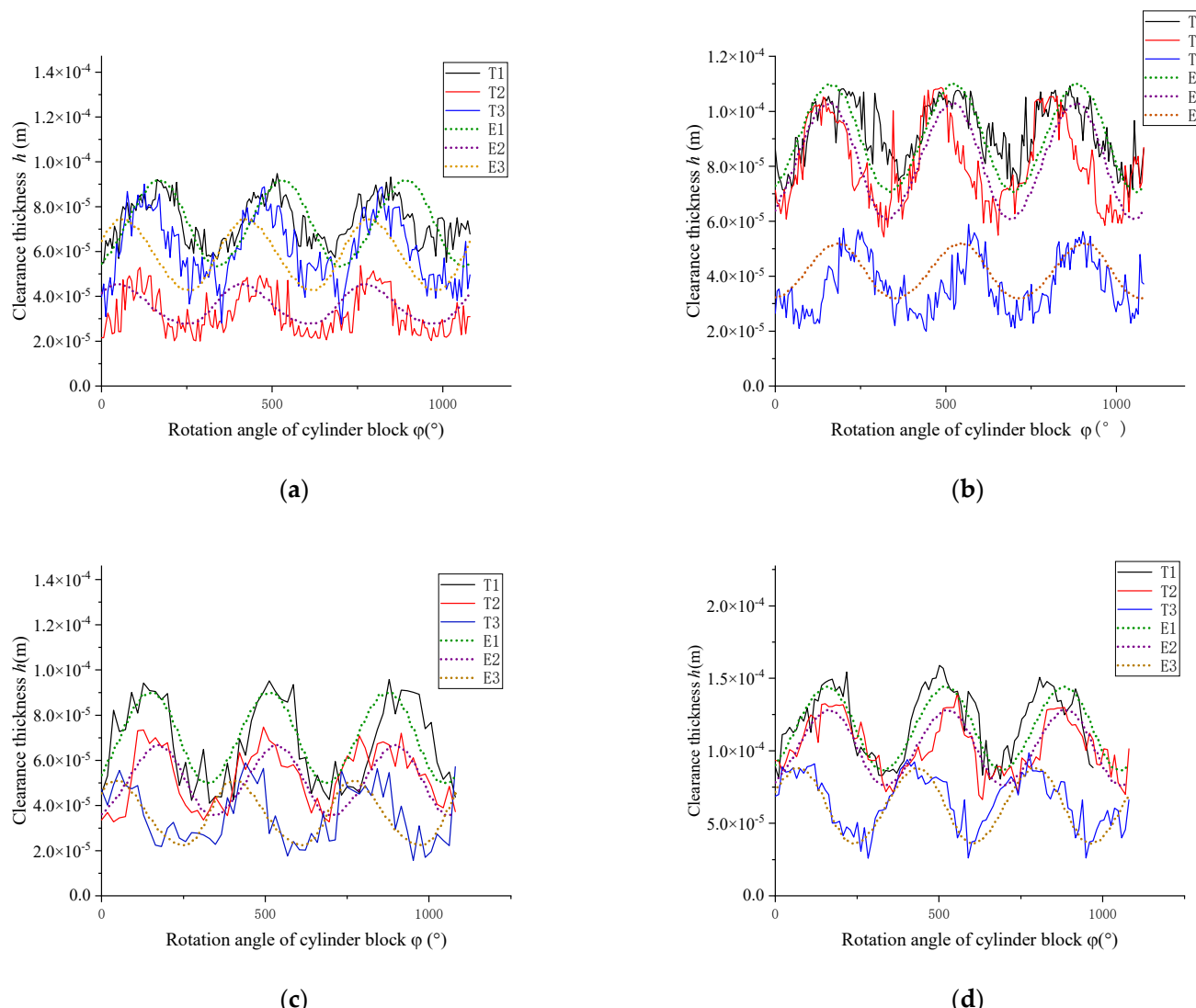


**Figure 13.** The gap thickness curves at test points T1, T2, and T3 at different working conditions: (a) condition 1; (b) condition 2; (c) condition 3; (d) condition 4.

All film thickness curves are trigonometric function curves at working conditions 1~4 in Figure 13. The three theoretical curves E1, E2, and E3 agree well with the three test curves T1, T2, and T3 under working conditions 1~4, respectively. At the same pump working pressure, the film thickness fluctuation amplitudes at the three test points in working conditions 1 and 2 are larger than those in working conditions 3 and 4. This indicates that the impact of the swash plate tilt angle on the total wedge angle and total azimuth angle of the lubrication film is larger than that of the pump working pressure. As the swash plate tilt angle is the same, the mean film thickness value of T1 and T2 in working condition 2

is less than that in working condition 1 as the working pressure increases. This indicates that the total wedge angle increases with higher pressure. We define the average error to describe the degree of coincidence between experimental and theoretical results. The average error is the difference between the average of all test values of the experiment and the average of the theoretical calculation data.

Figure 13a shows the theoretical and test curves of film thickness at the three test points at working condition 1. The average values of the test curves T1, T2, and T3 under working condition 1 are  $7.36 \times 10^{-5}$  m,  $3.26 \times 10^{-5}$  m, and  $6.12 \times 10^{-5}$  m, respectively, and their amplitudes are  $2.12 \times 10^{-5}$  m,  $2.11 \times 10^{-5}$  m, and  $2.88 \times 10^{-5}$  m, respectively. The average values of theoretical curves E1, E2, and E3 are  $7.26 \times 10^{-5}$  m,  $3.60 \times 10^{-5}$  m, and  $5.82 \times 10^{-5}$  m, respectively, and their amplitudes are  $1.91 \times 10^{-5}$  m,  $9.56 \times 10^{-6}$  m, and  $1.61 \times 10^{-5}$  m, respectively. The average errors of the three test curves and theoretical curves under working condition 1 are  $0.1 \times 10^{-5}$  m,  $0.34 \times 10^{-5}$  m, and  $0.3 \times 10^{-5}$  m, respectively.

Figure 13b shows the theoretical and test curves of film thickness at the three test points at working condition 2. The average values of the test curves T1, T2, and T3 under working condition 2 are  $9.24 \times 10^{-5}$  m,  $7.01 \times 10^{-5}$  m, and  $3.66 \times 10^{-5}$  m, respectively, and their amplitudes are  $1.68 \times 10^{-5}$  m,  $2.13 \times 10^{-5}$  m, and  $2.23 \times 10^{-5}$  m, respectively. The average values of theoretical curves E1, E2, and E3 are  $9.03 \times 10^{-5}$  m,  $7.08 \times 10^{-5}$  m, and  $4.15 \times 10^{-5}$  m, respectively, and their amplitudes are  $1.99 \times 10^{-5}$  m,  $1.69 \times 10^{-5}$  m, and  $1.05 \times 10^{-5}$  m, respectively. The average errors of the three test curves and theoretical curves under working condition 2 are  $0.21 \times 10^{-5}$  m,  $0.07 \times 10^{-5}$  m, and  $0.49 \times 10^{-5}$  m, respectively.

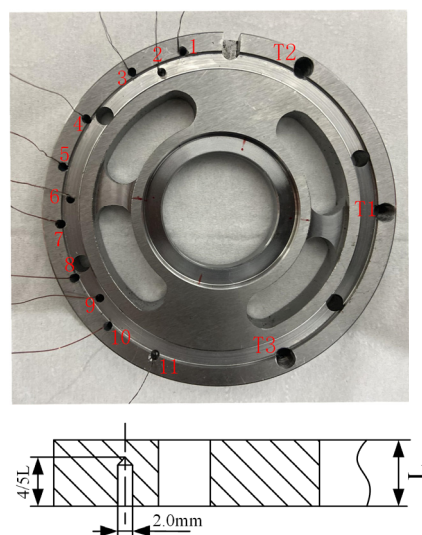
Figure 13c shows the theoretical and test curves of film thickness at the three test points at working condition 3. The average values of the test curves T1, T2, and T3 under working condition 3 are  $6.94 \times 10^{-5}$  m,  $5.26 \times 10^{-5}$  m, and  $3.55 \times 10^{-5}$  m, respectively, and their amplitudes are  $2.85 \times 10^{-5}$  m,  $1.98 \times 10^{-5}$  m, and  $1.97 \times 10^{-5}$  m, respectively. The average values of theoretical curves E1, E2, and E3 are  $7.01 \times 10^{-5}$  m,  $5.08 \times 10^{-5}$  m, and  $3.60 \times 10^{-5}$  m, respectively, and their amplitudes are  $2.02 \times 10^{-5}$  m,  $1.49 \times 10^{-5}$  m, and  $1.34 \times 10^{-5}$  m, respectively. The average errors of the three test curves and theoretical curves under working condition 3 are  $0.07 \times 10^{-5}$  m,  $0.18 \times 10^{-5}$  m, and  $0.05 \times 10^{-5}$  m, respectively.

Figure 13d shows the theoretical and test curves of film thickness at the three test points at working condition 4. The average values of the test curves T1, T2, and T3 under working condition 4 are  $1.20 \times 10^{-4}$  m,  $1.02 \times 10^{-4}$  m, and  $6.56 \times 10^{-5}$  m, respectively, and their amplitudes are  $3.89 \times 10^{-5}$  m,  $3.79 \times 10^{-5}$  m, and  $3.31 \times 10^{-5}$  m, respectively. The average values of theoretical curves E1, E2, and E3 are  $1.16 \times 10^{-4}$  m,  $1.02 \times 10^{-4}$  m, and  $5.92 \times 10^{-5}$  m, respectively, and their amplitudes are  $2.83 \times 10^{-5}$  m,  $2.59 \times 10^{-6}$  m, and  $2.61 \times 10^{-5}$  m, respectively. The average errors of the three test curves and theoretical curves under working condition 4 are  $0.04 \times 10^{-5}$  m, 0 m, and  $0.64 \times 10^{-5}$  m, respectively.

#### 4.2. Temperature Characteristics of the Valve Plate Oil Film

The highest film temperature of the valve plate pair appears in the auxiliary support belt due to the minimum-film-thickness point located in the auxiliary support belt. To protect the auxiliary support belt film and utilize the valve plate's high thermal conductivity, eleven holes for thermocouples are placed in the back of the auxiliary support belt in the high-pressure side in Figure 14. The diameter of every thermocouple hole is 2 mm, and its depth is four-fifths of the valve plate thickness. The temperature measured with a thermocouple in one hole was considered to be the oil film temperature at the corresponding point of the valve plate auxiliary support belt.

Figure 15 shows the theoretical temperature distribution in the highest-temperature area of the auxiliary support belt. The curve A is the temperature distribution along the inner side of the auxiliary support belt. The temperature first increases then decreases in the circumferential direction of the valve plate, and the highest temperature of about  $60^{\circ}\text{C}$  is near the middle of the range  $[-60^{\circ}, 60^{\circ}]$  of the valve plate. The temperature increases slightly in the radial direction from the inner side to the outer side of the auxiliary support belt.



**Figure 14.** Thermocouple installation diagram.

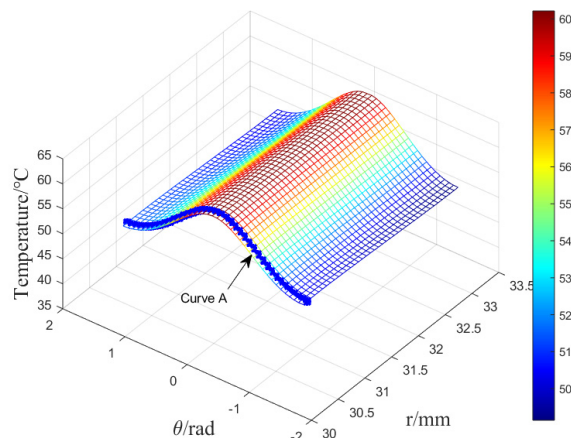


**Figure 15.** Temperature distribution in the highest–temperature area of the auxiliary support belt at working pressure 7 MPa and swash plate tilt angle 16°.

Figure 16 shows the theoretical calculation results of the temperature distribution along curve A in Figure 15 in the high-pressure side of the auxiliary support belt at working conditions 1~4. In Figure 16, the theoretical and experimental film temperature values agree with each other; however, the theoretical maximum film temperatures at working conditions 1~4 are always higher than the experimental values. It is probably because the thermocouples installed on the back of the valve plate cannot directly measure the gap in the film temperature between the cylinder block and the valve plate.

In Figure 16a, under working conditions 1 and 2, the experimental maximum film temperatures are 39.91 °C and 51.73 °C, and the theoretical values are 41.83 °C and 53.72 °C, respectively. The theoretical and experimental maximum film temperature errors at working conditions 1 and 2 are 1.92 °C and 1.99 °C, respectively. In Figure 16b, under working conditions 3 and 4, the experimental maximum film temperatures are 41.06 °C and 59.12 °C, and the theoretical values are 44.25 °C and 62.26 °C, respectively. The theoretical and experimental maximum film temperature errors at working conditions 3 and 4 are 3.19 °C and 3.14 °C, respectively. In Figure 16c, under working conditions 1 and 3, the gradient of experimental temperature curves is smaller than the theoretical temperature gradient in the circumferential range  $[-60^\circ, 60^\circ]$  of the valve plate. In Figure 16d, under working conditions 2 and 4, the gradient of experimental temperature curves is smaller than the theoretical temperature gradient in the circumferential range  $[-60^\circ, -20^\circ]$ . The gradients of

both experimental and theoretical temperature curves are very close in the circumferential  $[20^\circ, 60^\circ]$  range of the valve plate.

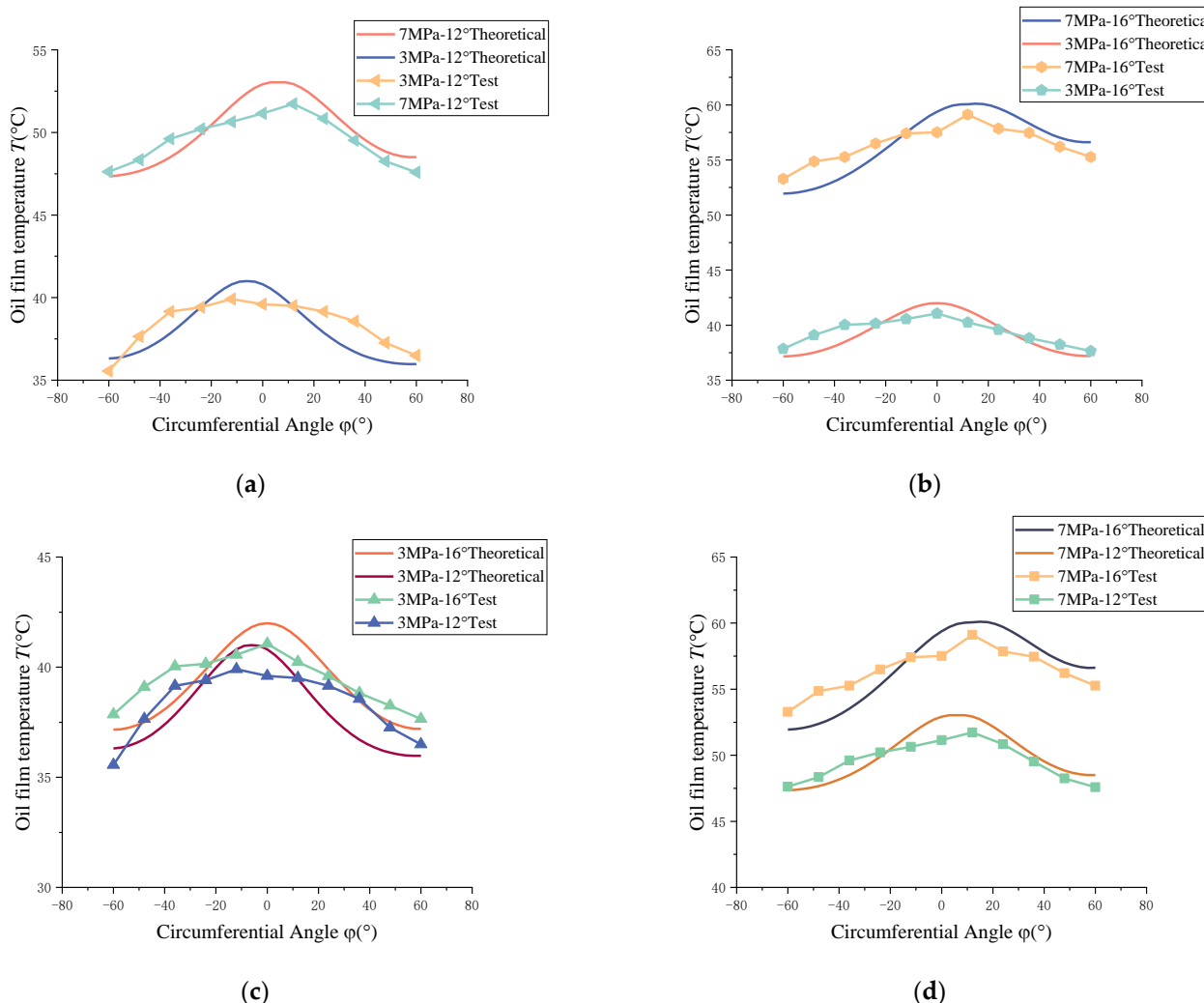


**Figure 16.** Film temperature distribution along the inner side of the auxiliary support belt at different working conditions: (a) conditions 1 and 2; (b) conditions 3 and 4; (c) conditions 1 and 3; (d) conditions 2 and 4.

It is seen in Figure 16a,b that the experimental and theoretical film temperatures in the high-pressure side of the auxiliary support belt increase with the increasing working pressure from 3 MPa to 7 MPa. This is because the pump pressure increase causes an increase in the film wedge angle, a decrease in the minimum film thickness, higher viscous friction loss, and more leakage loss in the valve plate pair. As the working pressure increases from 3 MPa to 7 MPa, the maximum temperature position moves from  $-15^\circ$  to  $5^\circ$  in the circumferential direction of the valve plate. This indicates that the working pressure increase would cause the azimuth angle to change from  $-15^\circ$  to  $5^\circ$  in the circumferential direction. The swash plate tilt angle increase causes a decrease in the minimum film thickness, more viscous friction loss, and higher film temperature.

## 5. Conclusions

In this paper, the temperature distribution of the valve plate pair in the axial piston pump was studied theoretically and experimentally. The main conclusions are as follows:

1. To improve the accuracy of the film temperature model, a test platform was built, in which three displacement sensors were installed in the low-pressure side of the valve

plate and eleven thermocouples were laid in the high-pressure side of the back of the valve plate. Based on the collected data from the three-point film displacement sensors, a film shape model of the valve plate pair was established, considering the effects of the fluctuation factor (coaxiality factor) and constant factors (force, moment, and off-wear factors). Then, the film temperature model was established, considering the viscosity–temperature characteristics of hydraulic oil, the energy loss caused by viscous friction and leakage, and the heat conduction among the oil, cylinder block, and valve plate. The theoretical and experimental film temperature results agree well with each other.

2. Film thickness tests were conducted under the working pressures of 3 MPa and 7 MPa, swash plate tilt angles of  $12^\circ$  and  $16^\circ$ , and a working speed of 1000 rpm. Under working condition 1 of 3 MPa and  $12^\circ$ , the average value error of the film thickness test curve and the theoretical curve is less than  $0.4 \times 10^{-5}$  m. Under working condition 2 of 3 MPa and  $16^\circ$ , their average value error is less than  $0.5 \times 10^{-5}$  m. Under working condition 3 of 7 MPa and  $12^\circ$ , their average value error is less than  $0.2 \times 10^{-5}$  m. Under working condition 4 of 7 MPa and  $16^\circ$ , their average value error is less than  $0.7 \times 10^{-5}$  m. The theoretical film thickness curves agree well with the experimental film thickness curves.
3. The film temperature increases with an increase in the working pressure and swash plate tilt angle. The absolute error between the test and theoretical results of the maximum oil film temperature in the valve plate pair is less than  $3.5^\circ\text{C}$ . As the working pressure increases from 3 MPa to 7 MPa and the swash plate tilt angle increases from  $12^\circ$  to  $16^\circ$ , the position of the highest-temperature point shifted from  $-15^\circ$  to  $5^\circ$  in the circumferential direction of the valve plate.
4. This manuscript also has some limitations. This manuscript does not take into account the effects of triangular grooving on the film of the valve plate pair and the effects of cavitation on the film forming of the valve plate pair. Theoretical modeling and testing were carried out under relatively low pressure, and no tests were carried out under relevant high-pressure and high-speed conditions.

**Author Contributions:** Conceptualization, Z.Z., S.M. and Z.L.; methodology, Z.Z. and S.M.; software, S.M. and Q.C.; validation, Z.Z., Q.C., L.L., S.M. and Z.L.; writing—original draft preparation, S.M.; writing—review and editing, S.M. and Z.Z.; supervision, Z.Z. and S.M.; data curation, S.M. and P.L. All authors have read and agreed to the published version of the manuscript.

**Funding:** This research has been supported by the National Natural Science Foundation of China (52175057), the Natural Science Foundation of Shanxi Province (20210302123215), and the special fund for Science and Technology Innovation Teams of Shanxi Province (202304051001033).

**Data Availability Statement:** The data are available upon request from the corresponding author. The data are not publicly available due to privacy.

**Conflicts of Interest:** The authors declare no conflicts of interest.

## References

1. Zhou, J.; Li, T.; Wang, D. A Novel Approach of Studying the Fluid–Structure–Thermal Interaction of the Piston–Cylinder Interface of Axial Piston Pumps. *Appl. Sci.* **2021**, *11*, 8843. [[CrossRef](#)]
2. Dašić, P.E.; Banaszek, A.; Turmanidze, E. The influence of tilt angle of the inclined plate on the gradient of the pressure increase in the piston axial pump cylinder. In Proceedings of the Fluid Power International Conference, Maribor, Slovenia, 21 September 2023.
3. Shin, J.-H.; Kim, H.-E.; Kim, K.-W. A Study on Models for the Analysis of Pressure Pulsation in a Swash-Plate Type Axial Piston Pump. *Tribol. Lubr.* **2011**, *27*, 314–320.
4. Azzam, I.; Pate, K.; Breidi, F.; Choi, M.; Jiang, Y.; Mousas, C. Mixed Reality: A Tool for Investigating the Complex Design and Mechanisms of a Mechanically Actuated Digital Pump. *Actuators* **2023**, *12*, 419. [[CrossRef](#)]
5. Chao, Q.; Zhang, J.H.; Xu, B.; Chen, Y.; Ge, Y.Z. Spline design for the cylinder block within a high-speed electro-hydrostatic actuator pump of aircraft. *Meccanica* **2018**, *53*, 395–411. [[CrossRef](#)]
6. Liu, G.; Zhou, Z.; Qian, X.; Wu, X.; Pang, W. Multidisciplinary Design Optimization of a Swash-Plate Axial Piston Pump. *Appl. Sci.* **2016**, *6*, 399. [[CrossRef](#)]

7. Boldyrev, S.V.; Budarova, O.P. Experimental study of wear of model friction pairs lubricated with contaminated oil. *J. Frict. Wear* **2016**, *37*, 346–350. [[CrossRef](#)]
8. Brazhenko, V. The influence of contaminated hydraulic fluid on the relative volume flow rate and the wear of rubbing parts of the aviation plunger pump. *Aviation* **2019**, *23*, 43–47. [[CrossRef](#)]
9. Duensing, Y.; Richert, O.; Schmitz, K. Investigating the Condition Monitoring Potential of Oil Conductivity for Wear Identification in Electro Hydrostatic Actuators. In Proceedings of the ASME/BATH 2021 Symposium on Fluid Power and Motion Control, ASME/BATH 2021 Symposium on Fluid Power and Motion Control, Virtual, 19–21 October 2021. V001T01A033.
10. Wang, Z.Q.; Hu, S.; Ji, H.; Wang, Z.; Liang, W. Study on the characteristics of oil film load capacity for axial piston pump. *Aust. J. Mech. Eng.* **2020**, *18*, 140–150. [[CrossRef](#)]
11. Wang, Z.Q.; Cheng, J.; Ji, H.; Hu, S.; Chen, H. Temperature characteristics analysis of axial piston pump port plate pair. *Ind. Lubr. Tribol.* **2019**, *71*, 603–609. [[CrossRef](#)]
12. Wang, Z.Q.; Hu, S.; Ji, H.; Wang, Z.; Liu, X.T. Analysis of lubricating characteristics of valve plate pair of a piston pump. *Tribol. Int.* **2018**, *126*, 49–64. [[CrossRef](#)]
13. Tang, H.S.; Ren, Y.; Xiang, J.W. A novel model for predicting thermoelastohydrodynamic lubrication characteristics of slipper pair in axial piston pump. *Int. J. Mech. Sci.* **2017**, *124*, 109–121. [[CrossRef](#)]
14. Tang, H.S.; Ren, Y.; Xiang, J.W. Power loss characteristics analysis of slipper pair in axial piston pump considering thermoelastohydrodynamic deformation. *Lubr. Sci.* **2019**, *31*, 381–403.
15. Bergada, J.M.; Watton, J.; Kumar, S. Pressure, flow, force, and torque between the barrel and port plate in an axial piston pump. *J. Dyn. Syst. Meas. Control-Trans. ASME* **2008**, *130*, 011011. [[CrossRef](#)]
16. Bergada, J.M.; Davies, D.L.; Kumar, S.; Watton, J. The effect of oil pressure and temperature on barrel film thickness and barrel dynamics of an axial piston pump. *Meccanica* **2012**, *47*, 639–654. [[CrossRef](#)]
17. Xu, H.G.; Zhang, J.H.; Sun, G.M.; Huang, W.D.; Huang, X.C. The direct measurement of the cylinder block dynamic characteristics based on a non-contact method in an axial piston pump. *Measurement* **2021**, *167*, 108279. [[CrossRef](#)]
18. Zhang, Z.Q.; Yuan, H.T.; Song, J.L.; Zhou, H.B. Modelling of the Micro Lubricating Gap Geometry between Valve Plate and Cylinder Block in an Axial Piston Pump. *Int. J. Fluid Power* **2020**, *21*, 211–234. [[CrossRef](#)]
19. Zhang, C.; Huang, S.K.; Du, J.; Wang, X.J.; Wang, S.P.; Zhang, H.Y. A new dynamic seven-stage model for thickness prediction of the film between valve plate and cylinder block in axial piston pumps. *Adv. Mech. Eng.* **2016**, *8*, 1687814016671446. [[CrossRef](#)]
20. Tang, H.S.; Yin, Y.B.; Ren, Y.; Xiang, J.W.; Chen, J. Impact of the Thermal Effect on the Load-Carrying Capacity of a Slipper Pair for an Aviation Axial-Piston Pump. *Chin. J. Aeronaut.* **2017**, *31*, 395–409. [[CrossRef](#)]
21. Kazama, T.; Tsuruno, T.; Sasaki, H. Temperature measurement of tribological parts in swash-plate type axial piston pumps. *Proc. JFPS Int. Symp. Fluid Power* **2008**, *2008*, 341–346. [[CrossRef](#)]
22. Zecchi, M.; Mehdizadeh, A.; Ivantysynova, M. A novel approach to predict the steady state temperature in ports and case of swash plate type axial piston machines. In Proceedings of the 13th Scandinavian International Conference on Fluid Power, Linköping, Sweden, 3–5 June 2013.
23. Zecchi, M. A Novel Fluid Structure Interaction and Thermal Model to Predict the Cylinder Block/Valve Plate Interface Performance in Swash Plate Type Axial Piston Machines. Ph.D. Thesis, Purdue University, West Lafayette, IN, USA, 2013.
24. Shang, L.; Ivantysynova, M. Port and case flow temperature prediction for axial piston machines. *Int. J. Fluid Power* **2015**, *16*, 35–51.
25. Chacon, R.; Ivantysynova, M. Thermal Effects on the Fluid Film in the Cylinder Block/Valve Plate Interface due to Compression and Expansion of the Fluid. *JFPS Int. J. Fluid Power Syst.* **2019**, *11*, 136–142. [[CrossRef](#)]
26. Petrović, R.; Banaszek, A.; Andjelković, M.; Qananah, H.R.; Alnagasa, K.A. Experimental Tests of the Piston Axial Pump with Constant Pressure and Variable Flow. *Designs* **2024**, *8*, 5. [[CrossRef](#)]
27. Zhang, Z.Q.; Chen, Y.Y.; Song, J.L.; Jin, K.S.; Zhou, H.B. Multiple frequency vibration of the micro lubricating gap geometry between cylinder block and valve plate in an axial piston pump. *J. Mech. Sci. Technol.* **2021**, *35*, 4835–4848. [[CrossRef](#)]
28. Deng, H.S.; Wang, Q.C.; Dai, P.; Yang, Y.K. Study on Leaking Characteristics of Port Plate Pair in Primary Three-Row Axial Piston Pump/Motor. *Math. Probl. Eng.* **2018**, *2018*, 7395727. [[CrossRef](#)]
29. Zhao, C.K.; Dong, H.K.; Wei, X.F.; Wang, D.Y.; Lu, X.P. Experimental study on the pressure distribution of piston/cylinder lubricating interface based on time domain location method. *Measurement* **2024**, *231*, 114595. [[CrossRef](#)]

**Disclaimer/Publisher’s Note:** The statements, opinions and data contained in all publications are solely those of the individual author(s) and contributor(s) and not of MDPI and/or the editor(s). MDPI and/or the editor(s) disclaim responsibility for any injury to people or property resulting from any ideas, methods, instructions or products referred to in the content.